Materials Research Express

PAPER

Effects of strain, defects and crystal phase transition in mechanically milled nanocrystalline In_2O_3 powder

Materials Research Express

PAPER

Effects of strain, defects and crystal phase transition in mechanically milled nanocrystalline In_2O_3 powder

M H Carvalho[1], M Rizzo Piton[1], O M Lemine[2], M Bououdina[3], H V A Galeti[4], S Souto[5], E C Pereira[6], Y Galvão Gobato[1] and A J A de Oliveira[1]

[1] Departamento de Física, Universidade Federal de São Carlos (UFSCAR), 13565-905, São Carlos, SP, Brazil
[2] Physics Department, Al Imam Mohammad Ibn Saud Islamic University (IMISU), College of Sciences, PO Box 90950, Riyadh 11623, Saudi Arabia
[3] Physics Department, Bahrain University, Bahrain
[4] Departamento de Engenharia Elétrica, Universidade Federal de São Carlos, 13565-905, São Carlos, SP, Brazil
[5] Departamento de Ciências Básicas—Faculdade de Zootecnia e Engenharia de Alimentos, Universidade de São Paulo, CEP 13635-900 Pirassununga, SP, Brazil
[6] Departamento de Química, Universidade Federal de São Carlos (UFSCAR), 13565-905, São Carlos, SP, Brazil

E-mail: yara@df.ufscar.br

RECEIVED
27 June 2018

REVISED
22 October 2018

ACCEPTED FOR PUBLICATION
29 October 2018

PUBLISHED
9 November 2018

Keywords: In_2O_3, x-ray diffraction, magnetic properties, photoluminescence, Raman spectroscopy

Supplementary material for this article is available online

Abstract

In this paper, we investigated structural, optical and magnetic properties of mechanically milled In_2O_3 nanoparticles in the cubic bixbyite phase. It was observed that mechanical milling induces an important increase in the density of defects, strain and hexagonal phase transition for cubic In_2O_3 nanoparticles. Remarkably, room temperature ferromagnetism was observed after mechanical milling. The hexagonal phase of In_2O_3 nanoparticles (H-In_2O_3) which is usually obtained in a high-temperature and pressure environment was clearly observed for the sample submitted to higher milling times which considerably affects the magnetic and optical properties. The physical origin of the FM order of mechanically milled In_2O_3 nanoparticles has been ascribed to the increase in the density of defects and strain.

1. Introduction

The observation of ferromagnetic order (FM) in undoped oxides has attracted much attention over the last years [1–10]. Its nature is usually associated to structural defects, such as oxygen vacancies and/or microstructural defects (lattice strain). Actually, the FM order was observed in different undoped semiconductor oxide systems, such as ZnO [1, 2], CeO_2 [3], HfO_2 thin film [4], ZnO nanoparticles [1], TiO_2 nanotubes, [5], CeO_2 nanoparticles [6] and electrodeposited thin films [7], SnO_2 thin films [8, 9], and In_2O_3 nanoparticles [10, 11]. Although these systems have not unpaired ions with *d* or *f* electron spins, they exhibit a ferromagnetic order even at room temperature. This magnetic behavior is usually called 'd^0 ferromagnetism' or defect-magnetism [12] and usually occurs in materials which do not have cations with partially filled *d* or *f* shells which is the condition for exchange interaction and consequently observation of ferromagnetism order.

In spite of all efforts, there is still a controversy considering its FM behavior of In_2O_3 and further studies are necessary to unveil the nature of this order in this oxide. For example, Sundaresan *et al* [13] and Cao *et al* [10] observed ferromagnetic behavior in In_2O_3 nanoparticles and attributed it to the presence of oxygen vacancies (V_0) at the surface of nanoparticles. Qaseem *et al* attributed the ferromagnetism in pristine indium oxide nanoparticles to the defect density and finite size effect [14]. However, previous studies of optical, structural, electrical and magnetic properties of In_2O_3 thin films grown by radiofrequency magnetron sputtering indicates that single ionized oxygen and indium vacancies are the key factors to mediate the ferromagnetism in this system [15]. Xiao *et al* has theoretically investigated states of the oxygen-depleted In_2O_3 (001) surfaces through first-principle density functional calculations. The authors assume that ferromagnetism arises from the interaction

between *In* s-p hybridization orbits [16]. Therefore, there are still several open questions associated to the effect of structural defects or vacancies in this oxide system.

In this paper, we have investigated the structural, morphological, optical, and magnetic properties of the cubic bixbyite phase of In_2O_3 nanoparticle samples prepared by mechanical milling processes for different times. Our studies were performed by using x-ray diffraction (XRD), high-resolution transmission electron microscopy (HRTEM), Raman spectroscopy, pPhotoluminescence (PL) and magnetization techniques. The samples have shown room-temperature ferromagnetism after mechanical milling. A hexagonal phase of In_2O_3 was also observed for the higher milled time sample. Our results have shown that mechanical milling has induced an important increase in intrinsic defects such as strain and oxygen and indium vacancies which result in room temperature FM in undoped In_2O_3.

2. Experimental details

Commercial In_2O_3 powder (purity: 99.9%) was milled under air in a planetary ball mill with milling time $t_m = 6, 12, 24, 48$ and 96 h. Zirconia grinding balls were used in order to avoid any contamination with magnetic impurities and the ball-to-powder mass ratio was fixed to 10:1. The crystalline structures of the samples were investigated by x-ray diffraction (XRD) using a Rigaku powder diffractometer (Model D/Max-2500PC) with CuKα radiation ($\lambda = 1.5418$ Å) and Bragg–Brentano geometry mode $\theta - 2\theta$ in the range of 10°–80° at a scan speed of 0.5°/min, with a step of 0.02°. Rietveld refinements [17] were performed using the free GSAS-EXPGUI software [18, 19]. The fitting procedure quality can be followed using the goodness of fit (S parameter), and it was described in the literature that if S is close to 1, it indicates an excellent fitting process [20]. The structure and size of the particles could be determined by the HRTEM technique, using a FEI microscope (model Tecnai G2 F20, FEI), operating at 300 kV.

Raman spectroscopy experiments were performed using a 514.5 nm laser and 0.5 m Andor spectrometer coupled with Si detector and appropriated filters. The estimated resolution is about 1.2 cm^{-1} and the Raman spectra was recorded in the range of 120 to 1600 cm^{-1} at room temperature. Macro-PL measurements were performed using a 500 M Spex spectrometer coupled with a GaAs PMT for the visible spectral region. A Kimmon He-Cd laser (line 325 nm) was used as the excitation source for PL measurements. For both measurements, the laser spot diameter on the sample is around 400 μm.

Magnetic properties were characterized by using a SQUID - VSM magnetometer (MPMS®3-Quantum Design). Magnetization measurements were performed as a function of the magnetic field in the temperature range from 5 to 300 K. Magnetization measurements as a function of temperature were performed with zero field cooled (ZFC) and field cooled (FC) protocols. The In_2O_3 samples were measured in squid using gelatin capsules supplied by Quantum Design. Extreme precautions were taken during this and other procedures to avoid contamination of the samples with magnetic impurities

3. Results and discussions

3.1. Structural and morphological properties

Figure 1 shows the evolution of the x-ray diffraction patterns (XRD) of In_2O_3 commercial powder, ($t_m = 0$ h) and milled at different times: 6, 12, 24, 48 and 96 h. The green vertical bars correspond to the indexation using the Inorganic Crystal Structure Database, (ICSD no. 41265) for the cubic bixbyite phase In_2O_3 (C-In_2O_3). All XRD standards shown in figure 1 indicate the same structure of C-In_2O_3, spatial group: ($Ia\bar{3}$), without the presence of any crystalline secondary phase in the range from 0 to 48 h. However, by increasing the milling time to 96 h, besides the C-In_2O_3, the new diffraction peak in the position around 32.7° appears (see asterisk in figure 1), indicating a phase transformation, promoted by the high energy condition. This peak can be indexed to the Bragg (110) peaks of the hexagonal structure (H-In_2O_3), spatial group: ($R\bar{3}c$) (ICSD No 016086). The observation of the phase transformation of C-In_2O_3 to H-In_2O_3 using a high-energy ball milling approach is in agreement with a previous study reported in the literature [21].

The XRD patterns for the samples 0 h and 96 h are shown in more detail in figure 2(a). The blue line corresponds to the difference between the experimental and calculated patterns using the Rietveld method [17]. A pseudo-Voigt function of Thompson-Cox-Hasting modified by Young and Desai (pV-TCHZ) as the profile function [22] was used in the fitting process. As can be observed, there is a broadening in the FWHM of the Bragg peaks and a decrease in the diffraction intensity as a function of the milling time. This variation in peak shape is related to a decrease in the average crystallite sizes (see table 1) and to structural distortion associated with the crystallinity of samples. In addition, a slight shift toward lower angles can be observed for longer milling time compared to commercial powder In_2O_3, as shown in figure 2(b), due generally to the expansion of the lattice [23]. In agreement, we observed an increase in the strain in the samples as a function of the milling time.

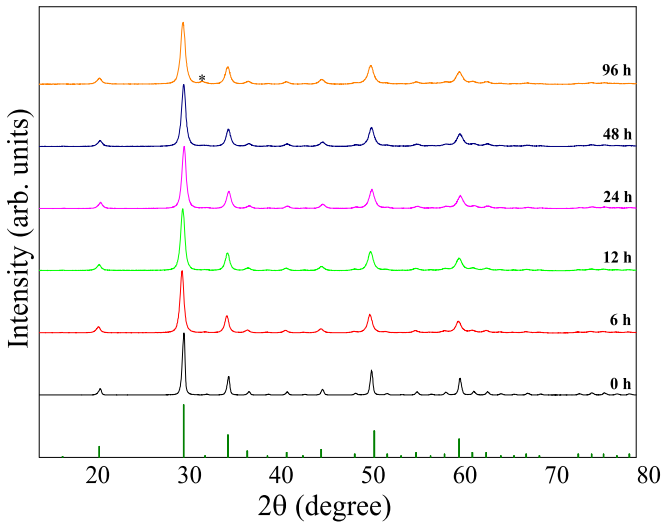

Figure 1. XRD patterns of commercial In_2O_3 powder and milled at different times. The green vertical bars correspond to the indexation for the In_2O_3 cubic phase (ICSD no. 41265).

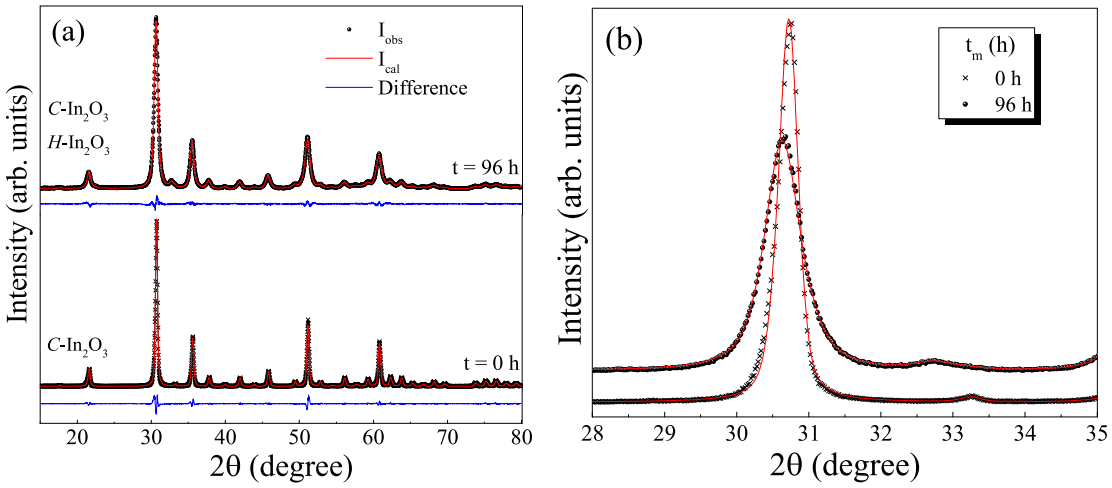

Figure 2. (a) XRD patterns of In_2O_3 commercial powder and milled at $t_m = 96$ h and (b) Details of XRD patterns around the highest intense peak. We remark that the highest intense peak which is associated to the plane (2 2 2) of phase C-In_2O_3 shows a shift after 96 h milling time. An overlap between the peaks (321) and (110) of the cubic and hexagonal phase of In_2O_3 was also observed, respectively, for the 96 h sample.

Table 1. Variation of crystallite size ($D_{x\text{-}ray}$), strain, lattice parameters with milling time as obtained by the Rietveld analysis.

	Lattice parameter (Å)					
Milling time (h)	$a = b$ (Å)	c (Å)	Cell volume V (Å^3)	$\langle D_{x\text{-}ray} \rangle$ (nm)	Strain (%)	S
0	10.1181 (2)	10.1181 (2)	1035.9 (6)	31.4	0.182	1.7
6	10.1364 (4)	10.1364 (4)	1041.5 (1)	17.2	1.538	1.6
12	10.1389 (4)	10.1389 (4)	1042.2 (1)	16.9	1.667	1.4
24	10.1376 (5)	10.1376 (5)	1041.8 (1)	17.3	1.793	1.4
48	10.1385 (5)	10.1385 (5)	1042.1 (1)	16.3	1.740	1.4
C-96[a]	10.1361 (4)	10.1361 (4)	1041.4 (1)	13.8	1.858	1.3
H-96	5.489 (1)	14.551 (6)	379.7 (1)	22.7	1.834	

[a] The percent weight for the cubic phase is 93.4% and for the hexagonal phase is 6.6% (96 h sample).

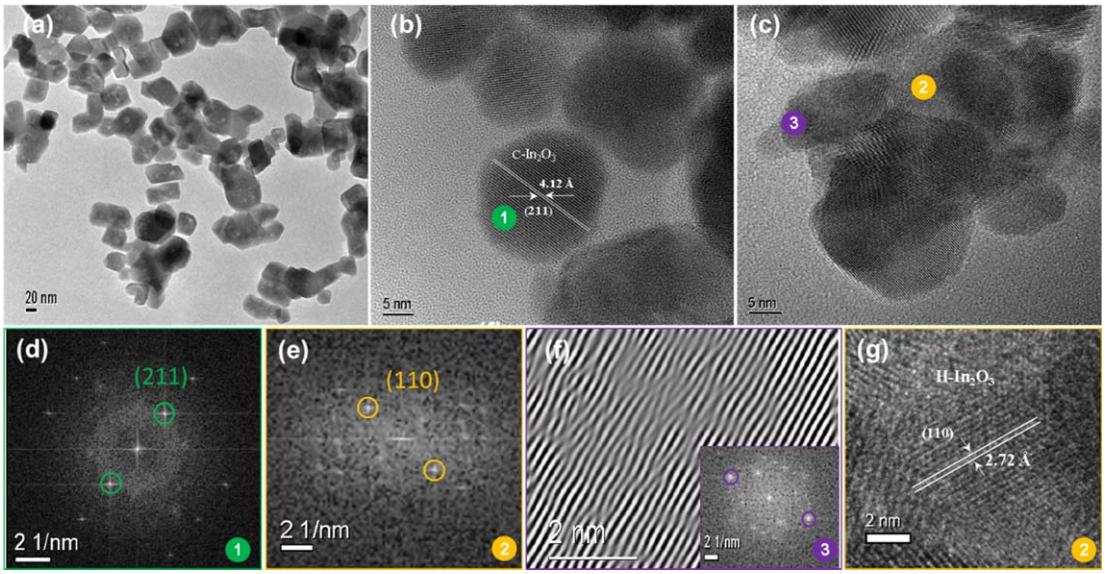

Figure 3. (a) TEM image for commercial In_2O_3 powder. (b), (c) HRTEM image with milling times of 24 h and 96 h, respectively. (d)–(e) FFT pattern referring to the cubic (C-In_2O_3) and hexagonal (H- In_2O_3). (f) Reconstructed HRTEM image of region 3, which shows the lattice mismatch between plans. (g) Magnification of region 2, showing the crystalline planes of the (H- In_2O_3).

The structural parameters calculated by the Rietveld refinement are listed in table 1, in which we present lattice parameters, unit cell volume, crystallite size $\langle D_{x\text{-}ray}\rangle$, lattice strain and goodness of fit values which is an indicator that the refinement quality is suitable. It can be observed that the lattice parameter (a) increases in the milling samples when compared to the pure one, while the crystallite size decreases 54.8% for $t_m = 6$ h. On the other hand, the strain increases with increasing milling time. Phan *et al* [2] reported similar behavior in milled ZnO nanoparticles for longer milling time and claimed that this is due to the appearance of V_{Zn} defects.

Figure 3 shows TEM images for In_2O_3 samples with different milling times: (a) 0 h, (b) 24 h and (c) 96 h. As can be seen from the low-magnification TEM image shown in figure 3(a), the sample commercial powder exhibits a morphology similar to nanocubes with an average particle size $\langle D\rangle = 36.4$ nm. However, with the milling process, the samples exhibit a clear spherical character (figures 3(b), (c)) with $\langle D\rangle = 18.1$ nm for the sample with $t_m = 24$ h and a bimodal particle size distribution, with $\langle D_1\rangle = 12\,(1)$ nm and $\langle D_2\rangle = 23\,(1)$ nm, for $t_m = 96$ h. In figure SI.4 (supplementary information is available online at stacks.iop.org/MRX/6/025017/mmedia), the particle size histograms obtained from several TEM images are presented. All histograms were adjusted by a log-normal distribution, with the exception of the sample with $t_m = 96$ h that fitted to a Bigaussian distribution. Performing fast Fourier transform (FFT) locally in regions 1, 2 and 3 reveals the distinct patterns shown in figures 3(d), (e) and inset figure 3(f). The patterns in figure 3(d) were observed in the HRTEM images in different regions in all samples, disclosing the lattice fringe spacing of 4.12 Å (see representation in region 1 figure 3(b)), which correspond to planes (211) lattice spacing of cubic In_2O_3. The pattern in figure 3(e) was observed only in the sample milling for 96 h and in a few regions, which we can infer corresponds to a minority phase. The lattice spacing of 2.72 Å (see the magnification of region 2 in figure 3(g)) can be observed, which corresponds to the plane (110) of the hexagonal structure (H-In_2O_3) in accordance with the results of XRD. Figure 3(f) shows the reconstructed HRTEM image of region 3 for the sample with 96 h of milling. It can be clearly observed that the sample has structural defects, observed in figure 3 by the lack of linear behavior of the crystalline planes.

3.2. Raman spectroscopy

Figure 4 shows the Raman spectra for different milling times. Five principal Raman peaks were observed at 134, 308, 366, 495 and 628 cm^{-1}. Less intense peaks at around 155, 172, 209, 213, 321 (shoulder), 407 and 594 cm^{-1} were also observed.

As discussed in the last section, the indium oxide compound has usually a cubic bixbyite-type (C-In_2O_3) crystal structure at room temperature and atmospheric pressure, and belongs to the $Ia\bar{3}$ space group with the point group T_h [24]. For this crystal structure, the following vibration modes are predicted as [24]:

$$4A_g + 4E_g + 14T_g + 5A_u + 5E_u + 16T_u$$

The vibrations with symmetry A_g, E_g, and T_g are Raman active, while T_u is infrared active and A_u and E_u are silent modes. Therefore, 22 Raman-active modes are expected to be observed for the C-In_2O_3 structure.

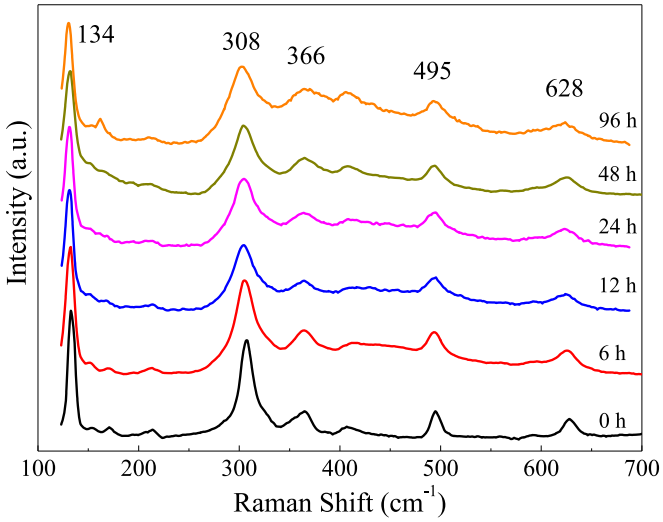

Figure 4. Raman scattering spectra for In_2O_3 nanoparticles for milling times: 0 h, 6 h, 12 h, 24 h, 48 h and 96 h.

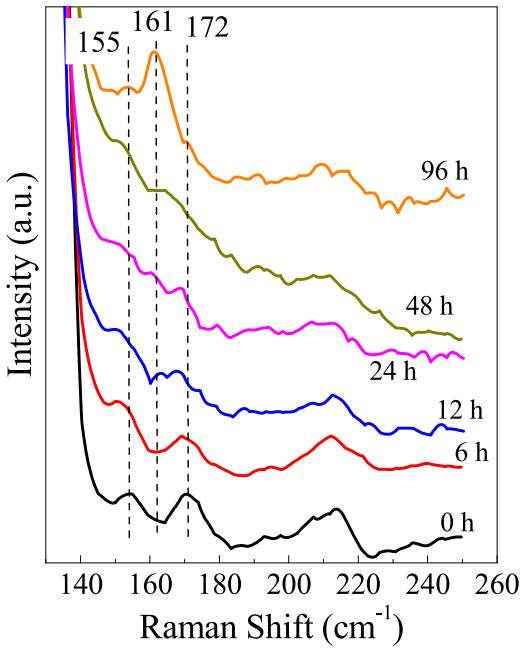

Figure 5. Raman scattering spectra in the range of 130 to 250 cm^{-1}.

However, only six (6) are generally observed at an average wave number at 110, 133, 306, 366, 496 and 630 cm^{-1} [24–27]. These values are close to the Raman peaks 134, 308, 366, 495 e 628 cm^{-1} observed in figure 4. Other peaks at 152, 154, 172, 205, 209, 211, 215, 317, 325, 396, 400, 589 and 590 cm^{-1} can also be observed for cubic bixbyite-type crystal structure [25–27]. These peaks are also close to the Raman peaks 155, 172, 209, 213, 321, 407 and 594 cm^{-1} observed in figure 4. Therefore, all observed Raman peaks are consistent with the cubic bixbyite-type (C-In_2O_3) crystal structure which were also evidence by XRD and TEM results.

Furthermore, Raman peaks due to the C-In_2O_3 crystal structure are observed for all milled samples. However, for some samples, these Raman peaks do not appear clearly mainly due to the increase of their linewidth and decrease of their intensity with the increase of milling time. On the other hand, the sample of 96 h milling time has clearly revealed an additional peak around 161 cm^{-1} which cannot be explained by the C-In_2O_3 crystal structure. Figure 5 shows the Raman spectra in the range of 130–250 cm^{-1}.

The hexagonal H-In_2O_3 crystal structure belongs to the space group $R\bar{3}c$, point group D_{3d}, with vibration modes [28, 29]:

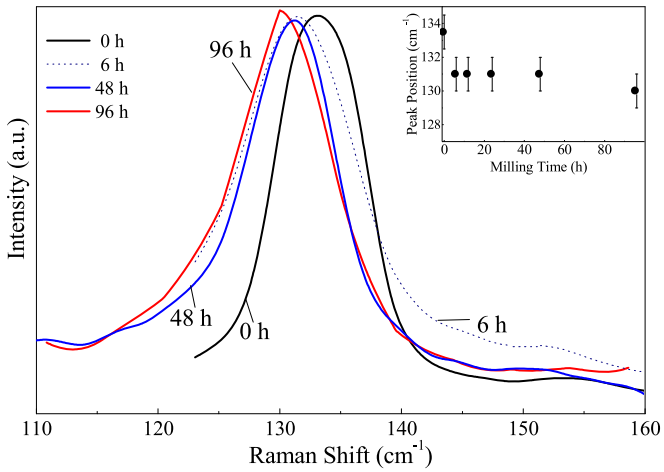

Figure 6. Normalized Raman peak around 134 cm^{-1} for the samples of 0, 6, 48 and 96 h of milling time. The inset shows the Raman peak position as a function of the milling time.

$$2A_{1g} + 2A_{1u} + 3A_{2g} + 2A_{2u} + 5E_g + 4E_u$$

The vibration modes with symmetry A_{1g} and E_g are only Raman active and A_{2u} and E_u are only infrared active and, A_{1u} and A_{2g} are silent modes. The Raman Scattering spectrum is expected to show 7 peaks. Experimental results for the hexagonal phase [28, 29] have shown that the Raman spectra is dominated by an intense peak at around 164 cm^{-1}, associated to the A_{1g}(TO) mode, followed by 5 or 6 less intense peaks. Although the Raman spectrum of the 96 h milling time has characteristic Raman peaks of the cubic C-In_2O_3 phase, the presence of the peak at 161 cm^{-1} indicates the presence of the hexagonal H-In_2O_3 phase for this sample in agreement to the XRD and HRTEM results which has also evidenced a hexagonal phase.

In addition, it was not observed any Raman peak related to impurities or to indium-related secondary phases after mechanical milling in good agreement with the XRD results and x-ray Photoelectron Spectroscopy (XPS) analysis (Supplementary Information).

It was observed that all Raman peaks showed a systematic red shift with the increase in milling time. This shift has different values for each Raman peak. Particularly, a red shift of about $\Delta\omega = 1.5$ cm^{-1} was observed for the 366 cm^{-1} peak and of about 6.0 cm^{-1} for the 308 cm^{-1} peak. Figure 6 shows the observed red shifts for the most intense and resolved Raman peak at around 134 cm^{-1}. Actually, previous Raman scattering studies [30–44] of several nanosystems have shown a systematic red shift ($\Delta\omega$) in the range of 1 to 10 cm^{-1}, with the decrease in the nanocrystallite size. Therefore, the observed red shift of Raman peaks for our In_2O_3 milled nanoparticles are fully consistent with previous reported values in the literature [30–33].

The nature of this red shift is not a consensus in the literature and was associated to different mechanisms: spatial confinement of phonons [35, 37–42]; strain-induced frequency change in phonon modes [25, 35, 36, 45–47]; defect-induced frequency change in phonon modes [10, 34, 35, 48]. However, two or more of these mechanisms can coexist in a complex interaction, whereas the parameters associated with these mechanisms are closely related. The observation of changes in crystallite size (in the nano-scale range) usually implies change in the microstrain, surface and crystalline defects. Therefore, a complex relationship among strain, size effect, phonon confinement and defects in the sample is expected.

The inset in figure 6 shows the dependence of the Raman peak observed around 134 cm^{-1} with the milling time. It was observed more important variation in the range 0 h to 6 h and a negligible variation with increasing milling time up or 96 h. This behavior is similar to the observed for XRD results for strain and crystallite size (figure SI.2 (*a*) e (*b*) presented in Supplementary Information).

Furthermore, as the milling time is increased, all Raman peaks have shown an important broadening, loose symmetry and decrease in intensity. These behavior evidence an increase of disorder in the crystalline structure, probably related to an increase in the density of defects which are mainly due to oxygen vacancies (V_O.).

Figure 7 show the full width half maximum (FWHM) of the Raman peak around 308 cm^{-1} as function of milling time. It was observed an increase of the FWHM with increasing milling time which is more pronounced in the range 0 h to 12 h.

In general, the XRD and Raman peak position have shown some structural changes with increase milling time only for samples milled for the range 0 h to 6 h and an incomplete transition phase for 96 h. However, the change of FWHM (figure 7) indicates that the long-range crystal order is affected during the whole milling process which evidences important formation of structural defects up to 12 h followed for a reduction in the

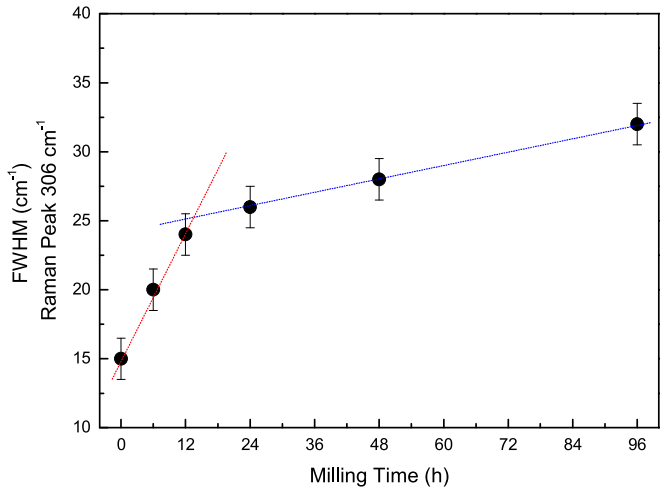

Figure 7. Raman Linewidth (FWHM) of the peak 306 cm^{-1} versus milling time. Dashed lines are guides for eye only.

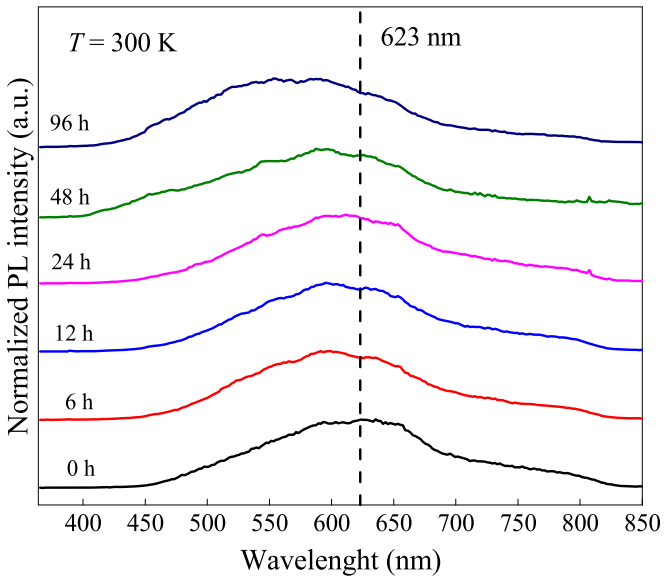

Figure 8. Room-temperature PL spectra of In_2O_3 nanoparticles for different milling times using laser excitation of 325 nm. The PL broad-band emission clearly shows a blueshift for the sample 96 h.

defect formation for higher milling times. This reduction of the increase of defects is probably due to the formation of the incipient hexagonal phase.

3.3. Photoluminescence

Figure 8 shows typical room-temperature macro-PL spectra of In_2O_3 powder under several ball-milling times. A broad-band red emission band was observed around 623 nm. This PL band is usually related to the defect emission which is due to the optical recombination related to defects (oxygen vacancy and/or indium vacancy levels) [49, 50]. Several previous papers for indium oxide thin films and nanowires [50–53] reported broad-band PL emission in the same spectral region, and were mainly ascribed to single ionized oxygen vacancies ($V_{\dot{O}}$). Although the laser excitation is 325 nm, we did not observe any evidence of near-band-edge emission, which is expected to be observed around 3 eV, probably due to a high density of defects in the In_2O_3 nanoparticles.

After mechanical milling, the samples have showed no important changes in the PL spectra excepted for the 96 h milling sample which showed an important shift to lower wavelength (blue shift) of PL peak position. Several different effects could result in a PL blue shift such as: quantum confinement [30], compressive strain [54] and a change to the hexagonal phase [55]. However, for the observed size of 20 nm, the contribution of the quantum confinement effect could be excluded. Concerning the effects of strain, it was shown previously that compressive strain usually increases the band gap of In_2O_3 [54]. However, our XRD results indicate a lattice

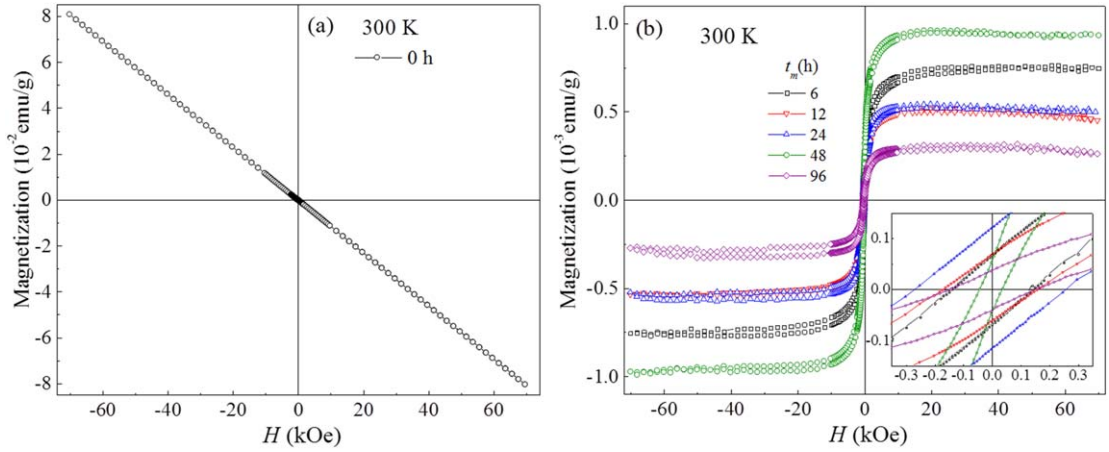

Figure 9. Magnetization curves as a function of the applied magnetic field, performed at 300 K for In_2O_3 NPs, (a) 0 h and (b) with t_m, 6, 12, 24, 48 and 96 h. The inset shows magnification of the low magnetic field region.

expansion. Therefore, a possible explanation for the observed blue shift of the PL band observed for the 96 h milled sample could be related to the appearance of the hexagonal phase (H-In_2O_3) which were evidenced by XRD, HRTEM and Raman results. Actually, as mentioned previously, the band gap of the hexagonal phase is higher than the cubic phase [55]. Therefore, the emission related to oxygen vacancies defects in hexagonal phase is expected to be at higher energy which could explain this small blue shift for the sample milled at 96 h.

In conclusion, our PL results have evidenced the presence of vacancy oxygen defects. In addition, the PL spectra have also showed important changes for the sample milled at higher times which could be explained by the formation of hexagonal phase.

3.4. Magnetic properties

Figure 9 shows the magnetization curves as a function of the applied magnetic field (*MvsH*), performed at 300 K, for NPs In_2O_3 with different milling times. Figure 9(a) show the *MvsH* curve at 300 K for the sample $t_m = 0$. We observe a clear diamagnetic behavior at 300 K. Figure 9(b) shows the *MvsH* curves (the diamagnetic contribution was subtracted) for the samples with t_m, 6, 12, 24, 48 and 96 h. The insets show enlargements of the curve region of the coercive field (H_C) and the remanent magnetization (M_r). All samples presented in figure 9(b) show a ferromagnetic behavior at room temperature, with saturation magnetization (M_S) of 0.757, 0.515, 0.527, 0.962 and 0.192 (10^{-3} emu g^{-1}) for the samples with t_m, 6, 12, 24, 48 and 96 h, respectively.

A quantitative explanation of the dependence of magnetic saturation with increasing milling time is a complex issue as it could depend on the increase of the density of defects, strain and the possible contribution of additional crystal phase. The dependence of the 300 K coercive field and the strain (obtained from the Rietveld refinement in XRD) as a function of the milling time are shown in figure 10, where both H_C and strain exhibit similar dependence. It was observed that the strain and coercive field values increase for samples milled up to 24 h. After that, both show a decrease to $t_m = 48$ h and an increase in the $t_m = 96$ h sample. The strain behavior up to $t_m = 24$ h can be associated with the increased dislocations density arising due to the elastic deformations during milling. From a certain density of dislocations, the regions strongly stressed in the crystal ends up dividing into smaller particles. In addition, with very small particles the deformation occurs by particle boundary sliding. However, beyond the time when the particle size reaches a saturation value, if there are still dislocation (since at very small grain sizes make it difficult for dislocations to arise), they will be rearranged and some will be annihilated [56]. Therefore, the lattice strain shows a reducing in value as happened with $t_m = 48$ h. The increase for the $t_m = 96$ h is related to the presence of the H-In_2O_3 phase.

The coercive field can be understood on the basis of Néel relaxation and the Bean-Livingston approaches, in which for an assembly of identical and non-interacting magnetic nanoparticles, follows the well-known relation:

$$H_C = \alpha \frac{2K_{eff}}{M_S}\left[1 - \left(\frac{T}{\langle T_B \rangle}\right)^{1/2}\right] \quad (1)$$

Where M_s is the saturation magnetization, $\langle T_B \rangle$ is an average blocking temperature, $\alpha = 0.48$ if the particles easy axis are randomly oriented or $\alpha = 1$ if aligned and K_{eff} is the constant of effective magnetic anisotropy [57, 58]. From the relation (1), we find that the coercive field is directly proportional to K_{eff}, which in our case, can be interpreted as a superposition of contributions from, surface anisotropy, magnetocrystalline, shape

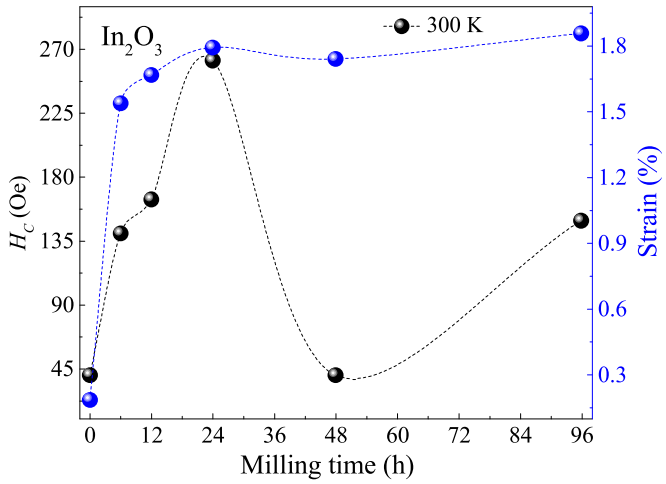

Figure 10. Coercive field and strain as a function of milling time for In_2O_3 NPs. The symbols represent the experimental data and the lines are a guide to the eye.

(magnetostatic energy) and stress (magnetoelastic energy) [59]. Although the relation (1) is widely used in the literature [60], it does not consider the existence of a size distribution, as in real particle systems. In systems with particle size distribution, the magnetization of the superparamagnetic particles whose portion increases with temperature, generates an average coercive field smaller than for the particle assembly that remain blocked, as proposed by Kneller and Luborsky [61].

Considering that the powders of In_2O_3 were milled in high-energy ball mills, we observed that our samples have high strain values (see figure 10), and as a consequence, exhibit large elastic stresses. Therefore, the magnetoelastic anisotropy energy may contribute to K_{eff}, which is directly proportional to H_c. In addition, the histograms obtained through the TEM images exhibit different particle size distributions (see figure SI.4), being that, the sample with $t_m = 48$ h having the thin size distribution. Consequently, at room temperature, a small fraction of blocked particles is responsible for the coercive field, in accordance with the decrease in *Hc* for this milling time.

Lastly, the behavior of the coercive field with increasing milling time is possibly the result of different contributions such as strain, particle size distribution and additional crystal phase.

To better understood the magnetic behavior of samples, magnetization measurements as a function of the temperature using the zero-field-cooled and field-cooled protocol (ZFC-FC) were performed with an applied magnetic field of 1 kOe over a wide temperature range ($5 \leqslant T \leqslant 350$ K) for the sample milled for 48 and 96 h, respectively, as show in figures 11(a), (b). It was observed that below 30 K, both samples exhibit an increase in the magnetization curve that can be associated with an alignment of non-interacting magnetic moments due to the application of the magnetic field, in agreement with magnetic behavior observed at 5 K in *MvsH* data. In addition, the ZFC and FC curves behavior shown in figure 11 exhibit a shoulder peak at $T_{máx}$ in the ZFC curve and the presence of thermal hysteresis (bifurcation between the ZFC and FC curves) at low temperatures, similar to the behavior generally observed in superparamagnetic systems. The inset in figure 11 shows a magnification of the ZFC-FC curves at high temperatures. In both samples, the ZFC and FC exhibit thermal irreversibility at 300 K, characteristic of a system with particle size distribution, in agreement with the particle size distributions obtained by TEM (see figure SI.4 (e) and (f)) and the hysteresis curves, *MvsH* at 300 K (see inset of figure 9(b)), which exhibit blocked particles. However, the sample with $t_m = 96$ h shows an irreversibility between the ZFC and FC curves even at 350 K. In addition, the ZFC and FC curves show two points of inflection suggesting the presence of two average blocking temperatures as a result of bimodal particle size distribution (see figure SI.4(f)).

The *MvsH* data measured with different temperatures for the sample milled for 48 and 96 h, respectively, are shown in figures 12(a), (b). For all curves, the diamagnetic contribution was subtracted. In the inset, we show the coercive field as a function of temperature. We observed that at a low temperature (5 K), the sample clearly exhibited both paramagnetic and ferromagnetic behavior. The paramagnetic behavior is due to the non-interacting magnetic moments associated with defects. The inset in figure 12(a) shows the temperature dependence of the coercive field for the sample milled at $t_m = 48$ h. This behavior agrees with the relation (1), in which a decay of the coercive field is expected with the square root of the temperature. Similar behavior occurs in the *MvsH* curves for samples with $t_m = 6$, 12 and 24 h (not shown here). However, the temperature dependence of the coercive field, $H_C(T)$ for the $t_m = 96$ h sample (inset of figure 12(b)) exhibits an unusual behavior with an increase up to a maximum around 100 K followed by a decrease. This unusual behavior can be interpreted on the

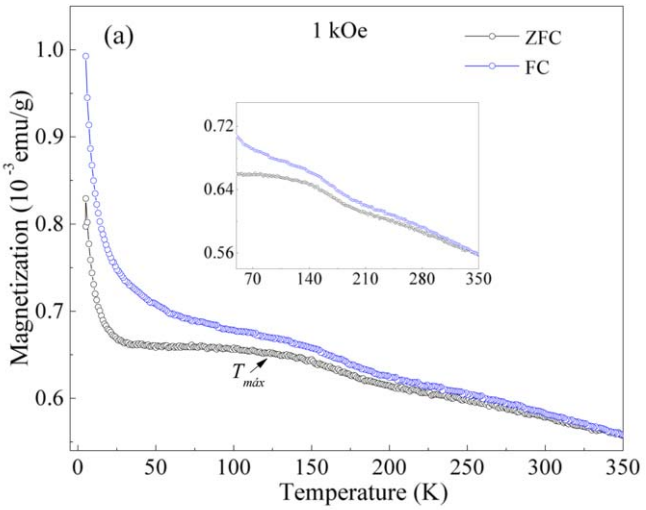

Figure 11. Magnetization curves as a function of temperature, ZFC-FC: (a) for the NPs In_2O_3 milled for 48 h and (b) for the NPs milled for 96 h. The inset shows amplification curves around 300 K.

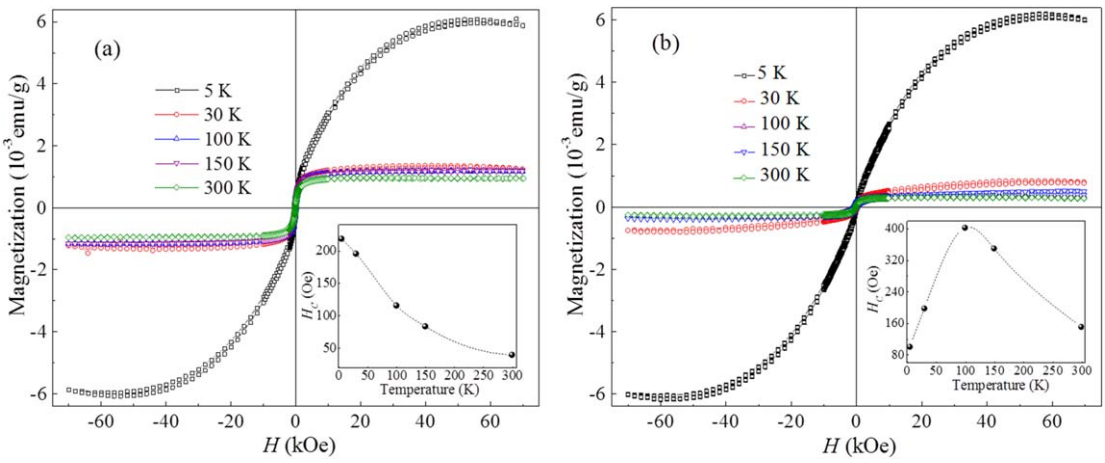

Figure 12. Magnetization curves as a function of the applied magnetic field for the NPs In_2O_3: (a) milled for 48 h and (b) milled for 96 h. The inset shows the temperature dependence on the coercive field.

basis of the large particle size distribution (see inset of figure 11(b)), as a consequence of the appearance of the hexagonal phase. Initially, with the application of the magnetic field, the smaller particles are unblocked up to 5 K, as the temperature increases the thermal fluctuations lead to a reduction of the superparamagnetic

susceptibility and consequently an increase of the $Hc(T)$ is observed. Finally, for temperatures greater than 100 K a large number of particles are unlocked leading to a reduction of $Hc(T)$.

4. Conclusions

Finally, our results of photoluminescence, magnetism, XRD, HRTEM and Raman show evidence of an important increase in the crystal structure disorder, mainly due to the increase in density of oxygen vacancies. The increase in intrinsic defects was associated to the observation of the ferromagnetism order in milled samples. In addition, the enhancement of local density of defects induces a change in cubic crystalline order favoring the growth of a new atomic arrangement. An increase in strain parameters was also observed, which was associated to the increase in the density of oxygen vacancy defects that locally reach a threshold and eventually form a hexagonal incomplete crystal phase (H-In_2O_3). This new crystal phase affects the optical and magnetic properties of the mechanically milled sample.

In conclusion, we performed a detailed study of optical, structural and magnetic properties of mechanical milled cubic bixbyite phase In_2O_3 nanoparticles. Diamagnetic behavior was observed for the commercial powder In_2O_3 sample. Room-temperature ferromagnetism was observed after mechanical milling. PL and Raman results have evidenced the presence of vacancy oxygen defects. In general, we have shown that mechanical milling induces a significant increase in the density of defects, strain and favors the formation of the hexagonal phase for In_2O_3 nanoparticles at higher milling times. In addition, it was observed that the hexagonal phase considerably affects the magnetic and optical properties (Raman and PL) of In_2O_3 nanoparticles. Finally, the physical origin of room temperature FM order has been ascribed to the increase in the density of intrinsic defects and strain after mechanical milling.

Acknowledgments

This work was supported by the FAPESP (grants 09/54082-2, 13/07296-2, 17/24995-2 and 16/106687), CAPES and CNPq Brazilian agencies. Thanks to CDMF (FAPESP N. 2013/07296-2, Brazil) for the XPS measurements. The authors acknowledge Prof. Renato V Gonçalves and Prof. Valmor R Mastelaro for the support of XPS measurements.

ORCID iDs

M H Carvalho https://orcid.org/0000-0002-5550-8202
M Rizzo Piton https://orcid.org/0000-0002-3972-7202
O M Lemine https://orcid.org/0000-0002-2516-3661
M Bououdina https://orcid.org/0000-0001-8770-7129
H V A Galeti https://orcid.org/0000-0002-5217-8367
Y Galvão Gobato https://orcid.org/0000-0003-2251-0426
A J A de Oliveira https://orcid.org/0000-0003-0145-9107

References

[1] Banerjee S, Mandal M, Gayathri N and Sardar M 2007 Enhancement of ferromagnetism upon thermal annealing in pure ZnO *Appl. Phys. Lett.* **91** 182501
[2] Phan T L, Zhang P, Yang D S, Thanh T D, Tuan D A and Yu S C 2013 Defect-induced ferromagnetism in ZnO nanoparticles prepared by mechanical milling *J. Appl. Phys.* **102** 072408
[3] Fernandes V *et al* 2010 Ferromagnetism induced by oxygen and cerium vacancies above the percolation limit in CeO_2 *J. Phys. Condens. Matter* **22** 216004
[4] Venkatesan M, Fitzgerald C B and Coey J M D 2004 Unexpected magnetism in a dielectric oxide *Nature* **430** 174117
[5] Alivov Y, Grant T, Capan C, Iwamoto W, Pagliuso P G and Molloi S 2013 Origin of magnetism in undoped TiO_2 nanotubes *Nanotechnology* **24** 275704
[6] Coey M, Ackland K, Venkatesan M and Sen S 2016 Collective magnetic response of CeO_2 nanoparticles *Nat. Phys.* **12** 694–9
[7] Fernandes V *et al* 2009 Dilute-defect magnetism: origin of magnetism in nanocrystalline CeO_2 *Phys. Rev.* B **80** 35202
[8] Chang G S, Forrest J, Kurmaev E Z, Morozovska A N, Glinchuk M D, McLeod J A, Moewes A, Surkova T P and Hong N H 2012 Oxygen-vacancy-induced ferromagnetism in undoped SnO_2 thin films *Phys. Rev.* B **85** 165319
[9] Hong N H, Poirot N and Sakai J 2008 Ferromagnetism observed in pristine SnO_2 thin films *Phys. Rev.* B **77** 33205
[10] Cao H, Xing P, Yao D and Wu P 2017 Annealing temperature dependent non-monotonic d^0 ferromagnetism in pristine In_2O_3 nanoparticles *J. Magn. Magn. Mater.* **429** 69–73
[11] Lemine O M, Bououdina M, Alyamani A, Omri K, Ibnaouf K and Ibrahem M A 2016 Defect-induced room temperature ferromagnetism in mechanically milled nanocrystalline In_2O_3 powder *Mater. Lett.* **181** 152–5
[12] Coey J M D 2005 Ferromagnetism *Solid State Sci.* **7** 660–7

[13] Sundaresan A, Bhargavi R, Rangarajan N, Siddesh U and Rao C N R 2006 Ferromagnetism as a universal feature of nanoparticles of the otherwise nonmagnetic oxides *Phys. Rev.* B **74** 161306
[14] Qaseem S, Ali S R, Naeem M and Rizvi S 2015 Size induced ferromagnetism in pristine indium oxide nanoparticles *Appl. Surf. Sci.* **331** 87–91
[15] Sun S, Wu P and Xing P 2012 d^0 ferromagnetism in undoped n and p-type In_2O_3 films *Appl. Phys. Lett.* **101** 1–5
[16] Xiao Z R, Fan X F, Guan L X, Huan C H A, Kuo J L and Wang L 2009 First-principles study of the magnetization of oxygen-depleted In_2O_3 (001) surfaces *J. Phys. Condens. Matter* **21** 272202
[17] Young R A 1995 *The Rietveld Method. IUCr (International Union of Crystallography)* (New York: Oxford University Press Inc.)
[18] Larson A C and von Dreele R B 2004 General structure analysis system (GSAS) *Los Alamos Natl. Lab. Rep. LAUR* 86–748 https://11bm.xray.aps.anl.gov/documents/GSASManual.pdf
[19] Toby B H 2001 EXPGUI, a graphical user interface for GSAS *J. Appl. Crystallogr.* **34** 210–3
[20] McCusker L B, Von Dreele R B, Cox D E, Louër D and Scardi P 1999 Rietveld refinement guidelines *J. Appl. Crystallogr.* **32** 36–50
[21] Liu D, Lei W, Qin S, Hou L, Liu Z, Cui Q and Chen Y 2013 Large-scale synthesis of hexagonal corundum-type In_2O_3 by ball milling with enhanced lithium storage capabilities *J. Mater. Chem.* A **1** 5274
[22] Young R and Desai P 1989 Crystallite size and microstrain indicators in rietveld refinement *Arch. Nauk. o Mater.* **10** 71–90
[23] Cullity B D and Stock S R 2001 *Elements of X-Ray Diffraction* (New Jersey: Prentice Hall)
[24] White W B and Keramidas V G 1972 Vibrational spectra of oxideswith the C-type rare earth oxide structure *Spectrochim. Acta* A **28** 501–9
[25] Liu D, Lei W W, Zou B, Yu S D, Hao J, Wang K, Liu B B, Cui Q L and Zou G T 2008 High-pressure x-ray diffraction and Raman spectra study of indium oxide *J. Appl. Phys.* **104** 83506
[26] Kranert C, Schmidt-Grund R and Grundmann M 2014 Raman active phonon modes of cubic In_2O_3 *Phys. Status Solidi - Rapid Res. Lett.* **8** 554–9
[27] Garcia-Domene B *et al* 2012 High-pressure lattice dynamical study of bulk and nanocrystalline In_2O_3 *J. Appl. Phys.* **112** 123511
[28] Wang C Y, Dai Y, Pezoldt J, Lu B, Kups T, Cimalla V and Ambacher O 2008 Phase stabilization and phonon properties of single crystalline rhombohedral indium oxide *Cryst. GROWTH &DESIGN 2008* **8** 1257–60
[29] Yu B D, Yu S, Zhang S, Zuo J, Wang D and Qian Y 2003 Metastable hexagonal In_2O_3 nanofibers templated from InOOH nanofibers under ambient pressure *Adv. Funct. Mater.* **13** 497–501
[30] Giri P K, Bhattacharyya S, Singh D K, Kesavamoorthy R, Panigrahi B K and Nair K G M 2007 Correlation between microstructure and optical properties of ZnO nanoparticles synthesized by ball milling *J. Appl. Phys.* **102** 093515
[31] Sendi R K and Mahmud S 2012 Quantum size effect on ZnO nanoparticle-based discs synthesized by mechanical milling *Appl. Surf. Sci.* **258** 8026–31
[32] Peleš A *et al* 2015 Structural investigation of mechanically activated ZnO powder *J. Alloys Compd.* **648** 971–9
[33] Živojinović J, Pavlović V P, Kosanović D, Marković S, Krstić J, Blagojević V A and Pavlović V B 2017 The influence of mechanical activation on structural evolution of nanocrystalline $SrTiO_3$ powders *J. Alloys Compd.* **695** 863–70
[34] Korotcenkov G, Boris I, Cornet A, Rodriguez J, Cirera A, Golovanov V, Lychkovsky Y and Karkotsky G 2007 The influence of additives on gas sensing and structural properties of In_2O_3-based ceramics *Sensors Actuators, B Chem.* **120** 657–64
[35] Popović Z V, Dohčević-Mitrović Z, Ŝćepanović M, Grujić-Brojčin M and Aŝkrabić S 2011 Raman scattering on nanomaterials and nanostructures *Ann. der Phys.* **523** 62–74
[36] Likodimos V, Chrysi A, Calamiotou M, Fernández-Rodríguez C, Doña-Rodríguez J M, Dionysiou D D and Falaras P 2016 Microstructure and charge trapping assessment in highly reactive mixed phase TiO_2 photocatalysts *Appl. Catal. B Environ.* **192** 242–52
[37] Curri M L, Agostiano A, Manna L, Monica M, Della, Catalano M, Chiavarone L, Spagnolo V and Lugarà M 2000 Synthesis and characterization of CdS nanoclusters in a quaternary microemulsion: the role of the cosurfactant *J. Phys. Chem.* B **104** 8391–7
[38] Richter H, Wang Z P and Ley L 1981 The one phonon Raman spectrum in microcrystalline silicon *Solid State Commun.* **39** 625–9
[39] Campbell I H and Fauchet P M 1986 The effects of microcrystal size and shape on the one phonon Raman spectra of crystalline semiconductors *Solid State Commun.* **58** 739–41
[40] Wang W and School L A 2008 Synthesis and optical properties of Mn_3O_4 nanowires by decomposing $MnCO_3$ nanoparticles in flux *Cryst. Growth {&} Des.* **8** 358–62
[41] Yin W, Su J, Cao M, Ni C, Cloutier S G, Huang Z, Ma X, Ren L, Hu C and Wei B 2009 $In(OH)_3$ and In_2O_3 Micro/nanostructures : controllable NaOAc-assisted microemulsion synthesis and raman properties *J. Phys. Chem.* C **113** 19493–9
[42] Su Y, Li G, Xue Y and Li P 2007 Tunable physical properties of $CaWO_4$ nanocrystals via particle size control *J. Phys. Chem.* C **111** 6684–9
[43] Wu X W, Wu D J and Liu X J 2008 Negative pressure effects in $SrTiO_3$ nanoparticles investigated by Raman spectroscopy *Solid State Commun.* **145** 255–8
[44] Aškrabiač S, Dohčeviač-Mitroviač Z, Kremenoviač A, Lazareviač N, Kahlenberg V and Popoviač Z V 2012 Oxygen vacancy-induced microstructural changes of annealed CeO_{2-x} nanocrystals *J. Raman Spectrosc.* **43** 76–81
[45] Olsen S H *et al* 2008 Nanoscale strain characterisation for ultimate CMOS and beyond *Mater. Sci. Semicond. Process.* **11** 271–8
[46] Pezzoli F *et al* 2008 Raman spectroscopy determination of composition and strain in heterostructures *Mater. Sci. Semicond. Process.* **11** 279–84
[47] Jain S C, Maes H E, Pinardi K and De Wolf I 1996 Stresses and strains in lattice-mismatched stripes, quantum wires, quantum dots, and substrates in Si technology *J. Appl. Phys.* **79** 8145
[48] Li B, Yu D and Zhang S-L 1999 Raman spectral study of silicon nanowires *Phys. Rev.* B **59** 1645–8
[49] Chan C H, Lin M H, Chao L C, Lee K Y, Tien L C and Ho C H 2016 Optical characterization of structural quality in the formation of In_2O_3 thin-film nanostructures *J. Phys. Chem.* C **120** 21983–9
[50] Kumar M, Singh V N, Singh F, Lakshmi K V, Mehta B R and Singh J P 2008 On the origin of photoluminescence in indium oxide octahedron structures *Appl. Phys. Lett.* **92** 171907
[51] Asok A, Gandhi M N and Kulkarni A R 2012 Enhanced visible photoluminescence in ZnO quantum dots by promotion of oxygen vacancy formation *Nanoscale* **4** 4943
[52] Tien L C and Hsieh Y Y 2014 Defect-induced ferromagnetism in undoped In_2O_3 nanowires *Mater. Res. Bull.* **60** 690–4
[53] Lee M, Choi W C, Kim E K, Kim C K and Min S 1996 *Characterization of the Oxidized Indium thin Films with Thermal Oxidation* **279** 1–3
[54] Walsh A, Catlow C R A, Zhang K H L and Egdell R G 2011 Control of the band-gap states of metal oxides by the application of epitaxial strain: the case of indium oxide *Phys. Rev. B - Condens. Matter Mater. Phys.* **83** 1–4
[55] King P D C *et al* 2009 Band gap, electronic structure, and surface electron accumulation of cubic and rhombohedral In_2O_3 *Phys. Rev. B - Condens. Matter Mater. Phys.* **79** 1–10

[56] Suryanarayana C 2001 Mechanical alloying and milling *Mater. Sci.* **46** 1–184
[57] Bean C P and Livingston J D 1959 Superparamagnetism *J. Appl. Phys.* **30** S120
[58] Stoner E C and Wohlfarth E P 1948 A mechanism of magnetic hysteresis in heterogeneous alloys *Philos Trans. R. Soc. London* **240** 599
[59] Cullity B D and Graham C D 1972 *Introduction To Magnetic Materials* (New York: Editora John Wiley & Sons)
[60] Carvalho M H, Lima R J S, Meneses C T, Folly W S D, Sarmento V H V, Coelho A A and Duque J G S 2016 Determination of the effective anisotropy constant of $CoFe_2O_4$ nanoparticles through the T-dependence of the coercive field *J. Appl. Phys.* **119** 093909
[61] Kneller E F and Luborsky F E 1963 Particle size dependence of coercivity and remanence of single-domain particles *J. Appl. Phys.* **34** 656 -